

## PAPER

# Accurate 3-Dimensional Imaging Method by Multi-Static RPM with Range Point Clustering for Short Range UWB Radar

Yuta SASAKI<sup>†</sup>, Fang SHANG<sup>†</sup>, Shouhei KIDERA<sup>†a)</sup>, and Tetsuo KIRIMOTO<sup>†</sup>, *Members*

**SUMMARY** Ultra-wideband millimeter wave radars significantly enhance the capabilities of three-dimensional (3D) imaging sensors, making them suitable for short-range surveillance and security purposes. For such applications, developed the range point migration (RPM) method, which achieves highly accurate surface extraction by using a range-point focusing scheme. However, this method is inaccurate and incurs great computation cost for complicated-shape targets with many reflection points, such as the human body. As an essential solution to this problem, we introduce herein a range-point clustering algorithm that exploits the RPM feature. Results from numerical simulations assuming 140-GHz millimeter wave-length radar verify that the proposed method achieves remarkably accurate 3D imaging without sacrificing computational efficiency.

**key words:** UWB radar, range points migration, multi-static UWB radar, millimeter wave radar, short range sensing

## 1. Introduction

The short range three-dimensional (3D) sensor that uses a millimeter wave radar system has an attractive attribute; it is applicable to optically harsh environments such as heavy smog or darkness. This feature promises various sensing applications, such as collision-avoidance sensor for vehicles and, watch sensors for independently living elderly or disabled persons. 140 GHz-band radar systems are attracting much attention, because this frequency range achieves low vapor absorption loss and enables automobiles to detect targets even in moisture-rich environments. Moreover, the transmitting and receiving modules can be very small, making implementation more flexible. There are many studies on establishing 3D imaging in short-range sensing, most of which are based on the delay-and-sum (DAS) approach, such as the synthetic aperture radar (SAR), time-reversal algorithms [1], or range migration methods [2]. However, the computational cost to obtain full 3-D images in these cases is very high, and continuous boundary extraction is inaccurate due to the point-wise target assumption. To counteract these effects, the non-parametric fast 3D imaging method SEABED (Shape Estimation Algorithm based on Boundary scattering transform and Extraction of Directly scattered waves) was developed. It is based on reversible transforms between the time delay and the target boundary [3]. However, this method has inherent drawbacks in that it requires

range points connection procedure as pre-processing, is difficult in environments with heavy interference. Moreover, SEABED suffers from inaccuracy caused by differences in range operation under noise or interference. Some studies developed a few array configurations for a Doppler radar system in order for it to create images of the human body [4], [5]. Using extracted Doppler-based range data and a simple spatial interferometer, people walking toward a radar installation were successfully reconstructed in less computational time. However, the direction of arrival (DOA) estimation made by this method suffers from some inaccuracies, which are caused by the mismatching of data paring among the arrays. This is because the method uses the simple spatial interferometer. Furthermore, the method requires complicated false image reduction processing using prior knowledge of the human body to perform the detection. The range-points migration (RPM) method was proposed to solve this problem [6]. This method is based on the target boundary extraction method, which considers the spatial relationship between the scattering center and its associated received sensors. A notable feature of this method is that it is applicable to richly interfered situations and incurs a low computational cost, because it does not require a connecting or paring procedure of range points prior to processing. Such processing is required by approaches using spatial interferometers, which therefore limits the usefulness of these approaches. Moreover, there are several extension studies on the RPM method for imaging of complicated shapes in real situations [7], interpolating SAR for industrial application [8], and acoustic biomedical imaging, especially for the surface extraction of a baby from the womb [9].

Herein the RPM method is extended to application in a 140-GHz millimeter-radar system with multistatic configuration. Notably, the multistatic configuration considerably reduces the data acquisition time compared to the radar scanning model, which is an important point for achieving real time imaging. However, in the case of multiple objects, the original RPM method still suffers from higher computational cost and inaccuracy. This is because, RPM determines the scattering center point for each corresponding range point using not only neighboring but a wider range of range points. Thus, with multiple objects, more range points must be processed, which greatly increases the computational cost. Some studies have modified the RPM algorithm, and in one such study, the optimal direction of arrivals was derived from the stationary point of the evaluation function [10]. This algorithm can accelerate the imag-

Manuscript received August 20, 2016.

Manuscript revised November 22, 2016.

Manuscript publicized January 27, 2017.

<sup>†</sup>The authors are with Graduate School of Informatics and Engineering, University of Electro-Communications, Tokyo, 182-8585 Japan.

a) E-mail: kidera@uec.ac.jp

DOI: 10.1587/transcom.2016EBP3327

ing process, but it may create inaccuracies due to capture by the local optimal solution. To overcome this issue, herein, range-points clustering is introduced during pre-processing. The more efficient correct range-points clustering reduces the unnecessary evaluation of the surrounding range points (hereafter referred to as Sub RPs,) and enhances the imaging accuracy using an appropriate set of Sub RPs. To further increase accuracy, this iteratively performs range-points clustering and RPM imaging. This iteration can be achieved by exploiting the unique RPM property that each target point is uniquely connected to each range point with one-to-one correspondence. Results obtained from geometrical optics (GO)-based numerical simulations indicate assuming 140 GHz millimeter wave radar system, that the proposed method remarkably enhances both computational cost and accuracy, compared with the original RPM.

## 2. System Model

Figure 1 shows the system model. It assumes that each target has an arbitrary 3D shape with a clear boundary, which is applicable to general artificial objects, such as walls and furniture. In addition, this assumption allows for a better understanding of discussing the reconstruction accuracy, which is defined as the position error of a reconstructed scattering center to an actual clear boundary. Omnidirectional antennas are arranged and fixed in an array on the  $y = 0$  plane to form a multistatic radar configuration, which considerably reduces the data acquisition time compared to the mono-static scanning model. The locations of the transmitting and receiving antennas are defined as  $L_T = (X_T, 0, Z_T)$  and  $L_R = (X_R, 0, Z_R)$ , respectively.  $s'(L_T, L_R, t)$  denotes the received electric field from the transmitting antenna  $L_T$  to the receiving antenna  $L_R$ , at time  $t$ .  $\tilde{s}(L_T, L_R, t)$  is the output of the Wiener filter of  $s'(L_T, L_R, t)$  calculated as;

$$\tilde{s}(L_T, L_R, t) = \int_{-\infty}^{\infty} W(\omega) S'(\omega) e^{j\omega t} d\omega, \quad (1)$$

In this equation,  $S'(L_T, L_R, \omega)$  is the signal in the frequency domain of  $s(L_T, L_R, t)$ .  $W(\omega)$  is defined as

$$W(\omega) = \frac{S_{\text{ref}}(\omega)^*}{(1 - \eta)S_0^2 + \eta|S_{\text{ref}}(\omega)|^2} S_0, \quad (2)$$

Here,  $\eta = 1/(1+(S/N)^{-1})$ , and  $S_{\text{ref}}(\omega)$  is the reference signal in the frequency domain, which is the complex conjugate of the transmitted signal.  $S_0$  is a constant that is used for dimensional consistency. This filter is an optimal MSE (Mean Square Error) linear filter for additive noises.  $\tilde{s}(L_T, L_R, t)$  is now converted to  $s(L_T, L_R, R')$  using  $R' = ct/2\lambda$ , where  $c$  is the speed of the radio wave in the air.  $q(L_T, L_R, R)$  is defined as the range point, which is extracted from the local maxima of  $s(L_T, L_R, R')$  to  $R'$ , more details are given in other studies [6].

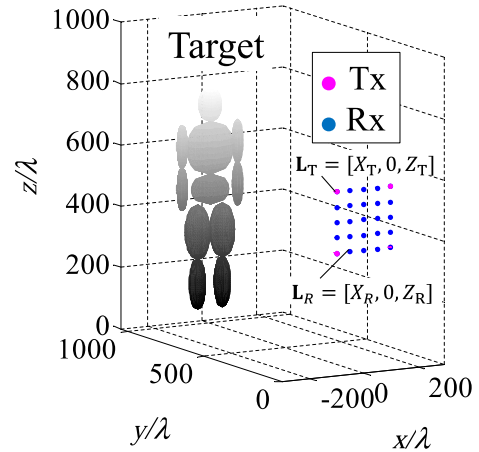


Fig. 1 System model.

## 3. Conventional 3D Imaging Methods

### 3.1 Delay-and-Sum Approach

Focusing on 3D short-range imaging, various target shape reconstruction methods were proposed based on the DAS approach. SAR is one of the most powerful tools even in short-range sensing. Although the SAR or other DAS approaches, such as the time-reversal or the range-migration methods, provide accurate an image of a point-wise target, they cannot offer sufficient accuracy for non-point-wise targets. This is because this type of approach assumes that all sensor locations could receive an echo from the same scattering center of an object, which is only valid for pointwise-shaped objects. In non-pointwise-shaped targets, such as those having smooth surfaces, a scattering center on an object boundary should move along a receiver location; i.e., data focusing using data from all sensor locations will cause a misplacement of the actual scattering center. Moreover, the incurred computational cost becomes enormous in 3D imaging due to the signal synthesizing approach with all received signals in each voxel evaluation.

### 3.2 Original Multi-Static RPM Method

The RPM method was established to overcome the above issues [6], it was extended to the multistatic observation model [11]. This method assumes that a target boundary point exists on an ellipsoid, whose focal points are  $L_T$  and  $L_R$  and its major radius is  $R$ . For extracting the target point, this method employs the basis that the actual target boundary point should be included in all the possible intersection points determined by other range points. Figure 2 shows the principle of the original multistatic RPM. For determining a target point  $p(q_i)$  corresponding to range point  $q_i$ , this method extracts the optimal intersection points by assessing the spatial accumulation of intersection points calculated by other range points (called SubRPs) as;

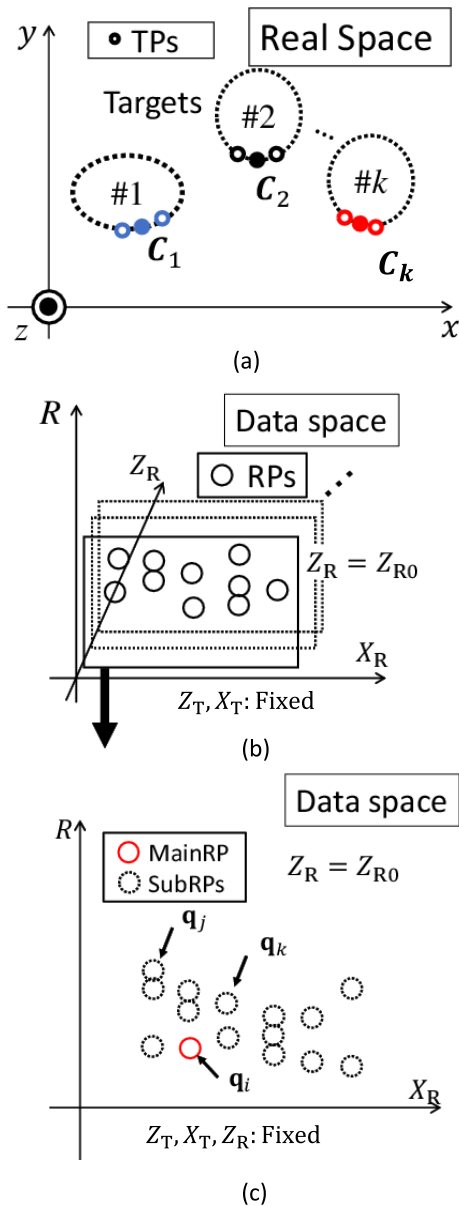


**Fig. 2** Relationship of the data space and the real space, and the MainRP and Sub RPs. (a) shows scattered center locations for each target, (b) shows the range point distribution in the extracted data space, where  $L_T$  is fixed, and (c) shows the extracted view, where  $L_T$  and  $Z_R = Z_{R0}$  are fixed, and the relationship between the MainRP and SubRPs.

$$\hat{p}(\mathbf{q}_i) = \arg \max_{\mathbf{p}^{\text{int}}(\mathbf{q}_i; \mathbf{q}_j, \mathbf{q}_k) \in \mathcal{P}_i} \sum_{(\mathbf{q}_j, \mathbf{q}_k) \in \mathcal{Q}_i} g(\mathbf{q}_i; \mathbf{q}_j, \mathbf{q}_k) \times \exp \left\{ -\frac{\|\mathbf{p}^{\text{int}}(\mathbf{q}_i; \mathbf{q}_j, \mathbf{q}_k) - \mathbf{p}^{\text{int}}(\mathbf{q}_i; \mathbf{q}_l, \mathbf{q}_m)\|}{2\sigma_r^2} \right\}, \quad (3)$$

where  $\mathbf{p}^{\text{int}}(\mathbf{q}_i; \mathbf{q}_j, \mathbf{q}_k)$  and  $\mathcal{P}_i$  denote the intersection points among the three ellipsoids and its set, respectively; these points are determined by the range points  $\mathbf{q}_i$ ,  $\mathbf{q}_j$ , and  $\mathbf{q}_k$ , and  $\mathcal{Q}_i$  denotes a set of SubRPs.  $\sigma_r$  determines the acceptable range of the intersection points, and is chosen by considering the spatial density of the accumulated intersection

points. The weighting function  $g(\mathbf{q}_i; \mathbf{q}_j, \mathbf{q}_k)$  is defined as follows:

$$g(\mathbf{q}_i; \mathbf{q}_j, \mathbf{q}_k) = s(\mathbf{q}_j) \exp \left\{ -\frac{D(\mathbf{q}_i, \mathbf{q}_j)}{2\sigma_D^2} \right\} + s(\mathbf{q}_k) \exp \left\{ -\frac{D(\mathbf{q}_i, \mathbf{q}_k)}{2\sigma_D^2} \right\}, \quad (4)$$

where  $\sigma_D$  determines the acceptable range for selecting SubRPs in terms of antenna location, and it is determined empirically.  $D(\mathbf{q}_i, \mathbf{q}_j)$  denotes the actual separation of the two sets of transmitting and receiving antennas as;

$$D(\mathbf{q}_i, \mathbf{q}_j) = \min \left( \|L_{T,i} - L_{T,j}\|^2 + \|L_{R,i} - L_{R,j}\|^2, \|L_{T,i} - L_{R,j}\|^2 + \|L_{R,i} - L_{T,j}\|^2 \right). \quad (5)$$

Notably, in this method, each range  $\mathbf{q}_i$  is related to a target point  $\mathbf{p}(\mathbf{q}_i)$ , with one-to-one correspondence. This method does not require range points connection before processing, achieving accurate conversion from range points to target points even in richly interfered cases. The RPM evaluates the accumulation degree of intersection points of ellipsoids defined by other range points (as SubRPs,  $\mathbf{q}_j$ ;  $\mathbf{q}_k$  in Eq. (1)). Figure 2 shows the relationship between the real and data spaces in a multi-static configuration, and Fig. 2(a) shows the scattered center locations for each target. Figure 2(b) shows the distribution of the range points extracted by the Wiener filter processing, which was described in Sect. 2. The range point denoted by  $\mathbf{q}(L_T, L_R, R)$  is a function of  $(L_T, L_R) = (X_T, Z_T, X_R, Z_R)$ . For clarity, the data space is extracted as the function  $(X_R, Z_R)$ , where  $L_T$  is fixed in the middle of Fig. 2. Figure 2(c) also shows the extracted view, where  $L_T$  and  $Z_R$  are fixed, as well as the relationship between the MainRP and SubRPs. As shown in this figure, each antenna receives a maximum of three RPs. In RPM, each focused RP (called Main RP) is evaluated by using surrounding all RPs (Sub RPs). However, in this evaluation, the number of SubRPs seriously affects a computational cost due to numerical solution for intersection point of three ellipsoids.

## 4. Proposed Method

### 4.1 Acceleration by Range Points Clustering

To solve the aforementioned problem, we introduce here the range-points clustering technique to eliminate the unnecessary SubRPs. In terms of computational efficiency and accuracy, the evaluated Sub RPs are included in the same target cluster of Main RP. In multiple target cases, if the Main RP corresponds to the target point in the  $n$ -th target (denoted as MainRP $_n$ ), the SubRPs also should correspond to those of the  $n$ -th target (denoted as SubRP $_n$ ). Figure 3 shows an example of correctly clustered range points. For an accurate and fast reconstruction of target points, only a set of SubRP is needed to evaluate MainRP $_n$  as the use of other RPs could introduce errors into the final image. However, it is difficult

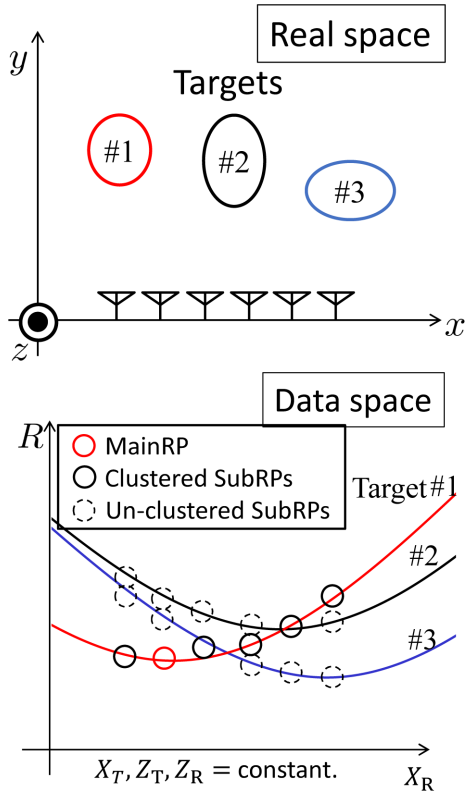


Fig. 3 Example of clustered data space.

to recognize the target number for each range point beforehand and without any prior knowledge. Furthermore, it is in general risky to ascertain the range point clustering without any prior knowledge of the target. As such, the proposed method introduces an initial estimation of the target points using RPM with far fewer (i.e., thinned out) range points. After a limited number of target points are acquired, they are clustered together using clustering algorithms, such as the agglomerative hierarchical clustering algorithm [11]. Next, using the clustered target points, all range points denoted as  $q_i$  are clustered as  $\mathcal{K}(q_i)$  by the following equation:

$$\mathcal{K}(q_i) = \arg \min_k (|\tilde{R}_{C_k}(L_{T,i}, L_{R,i}) - R_i|), \quad (6)$$

where  $C_k$  denotes a gravity center location of target points clustered as  $k$ , and  $\tilde{R}_{C_k}(L_{T,i}, L_{R,i})$  is defined as:

$$\tilde{R}_{C_k}(L_{T,i}, L_{R,i}) = \|C_k - L_{T,i}\|_2 + \|C_k - L_{R,i}\|_2. \quad (7)$$

Figure 4 shows an example of the determination process used for range point clustering, which was outlined in Eq. (6). Figure 4(a) shows the initially selected RPs (solid black circles) in the data space. Figure 4(b) illustrates the target points (hollow circles) obtained by RPM for selected RPs as well as a gravity point (solid circles) in each cluster. Figure 4(c) shows the actual clustering process by comparing the distance defined in Eq. (7) for non-selected RPs in the initial stage, where the solid curve denotes the predicted range curve assumed in each gravity point clustered in (b).

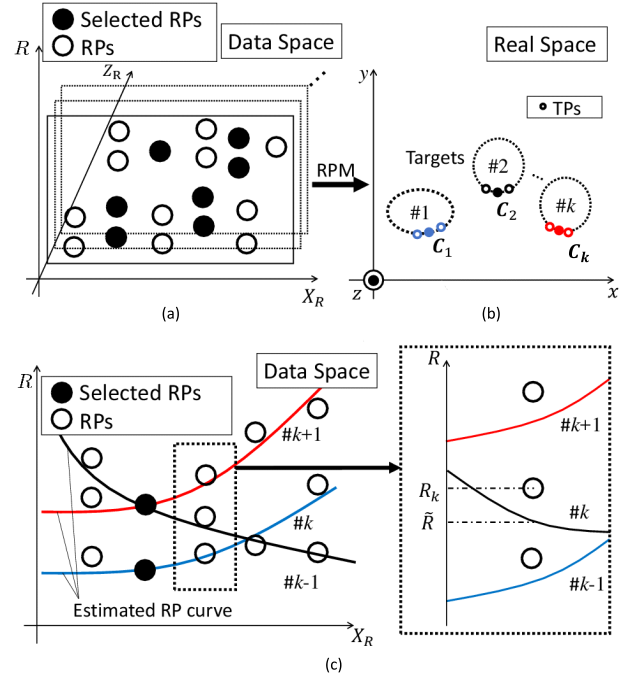


Fig. 4 Determination process for RPs clustering. (a) shows the initially selected RPs in data space, (b) illustrates the target points obtained by RPM for selected RPs, and (c) shows the clustering scheme for not selected RPs by using the target points obtained in (b) on data space.

While the RP clustering scheme assumes a point-wise target, the proposed method could reconstruct not only point-wise targets, such as flat bodies, because the imaging process after RP clustering is based on the original RPM.

To enhance further imaging accuracy of estimated target points, this method carries out the RPM imaging and range points clustering via target clustering, iteratively. Using the property of one-to-one correspondence between target point and range point, the cluster number of the range points in data space are directly related to that of target point in real space. By iterative application of RPM and range points clustering, the accuracy of clustering is expected to be improved, and it also enhances the accuracy for RPM imaging. Figure 5 shows the flowchart of the proposed RPM.

#### 4.2 Procedure of the Proposed Method

The procedure is as follows:

- Step 1) Observed data are acquired and are filtered by the Wiener filter as  $s(L_T, L_R, R')$ .
- Step 2) Range points  $q_i$  are extracted from  $s(L_T, L_R, R')$ , and a set of all RPs is defined as  $Q_{all}$ .
- Step 3) Initial target points (a set of them is denoted as  $\mathcal{T}_{sel}$ ) for clustering are determined by multistatic RPM with selected range points, a set of which is defined as  $Q_{sel}$  satisfying  $Q_{sel} \subset Q_{all}$ .
- Step 4) All target points included in  $\mathcal{T}_{sel}$  are clustered.
- Step 5) All range points included in  $Q_{all}$  are clustered with the clustered target points  $\mathcal{T}_{sel}$  in Eq. (6).

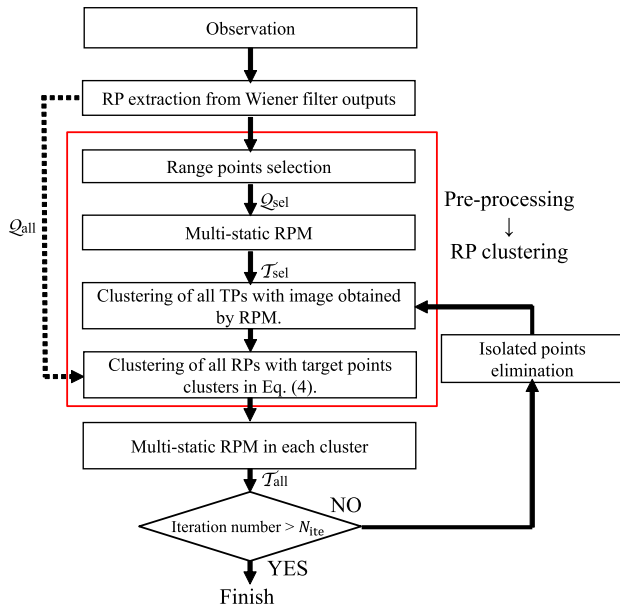


Fig. 5 Flowchart of the proposed method.

- Step 6) All range points are converted to target points with RPM method, a set of which is denoted as  $\mathcal{T}_{\text{all}}$ .  
 Step 7) Steps 4)–6) are repeated by the certain times.

Figure 5 shows the flowchart of the proposed RPM.

## 5. Evaluation in Numerical Simulation

This section investigates the performance evaluation of the conventional and the proposed methods in numerical simulation. The transmitted signal is set as a pulse modulated signal. The effective bandwidth is set to 10 GHz and its theoretical range resolution in the air is 15 mm. The center frequency is 140 GHz and its wavelength is 2.1 mm. The agglomerative hierarchical clustering method is used as an appropriate clustering algorithm for the target points. It assumes that the target is a human body; an aggregate of 11 ellipsoids corresponding to the head, upper and lower body, arms, and legs are used to represent this body (Fig. 1). Its center axis is located along  $x = 0$  and  $y = 1000\lambda$ . The numbers of transmitting and receiving antennas are 4 and 25, respectively. The array arrangement is also shown in Fig. 1, where the minimum array spacing is  $50\lambda$  and the center of the array locations is set to  $(x, y, z) = (0, 0, 500\lambda)$ . The received data are generated by geometrical optics (GO) approximation.

### 5.1 Noiseless Case

The images generated by SAR are shown in Fig. 6 for comparison, where the back projection algorithm is used [12]. The complex signal is obtained by applying the Hilbert transformation. Figure 6 also shows a cross-section image reconstructed by SAR, where each voxel size is set at  $1.0\lambda$ . Here, we apply a back projection based algorithm for 3-D

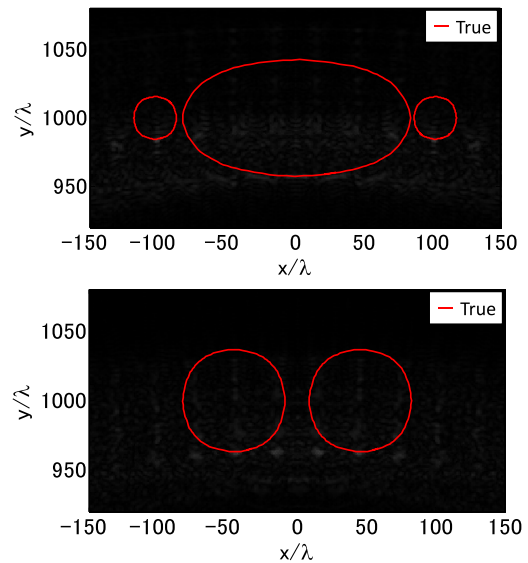


Fig. 6 Cross-section image of SAR,  $z = 560\lambda$  (upper, around torso and arms) and  $z = 330\lambda$  (lower, around thighs).

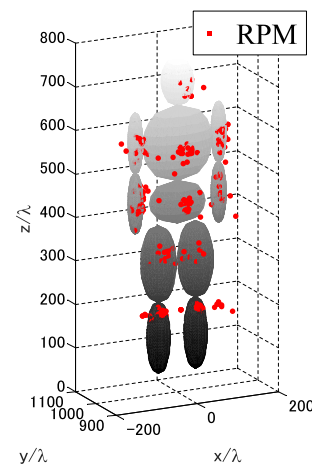
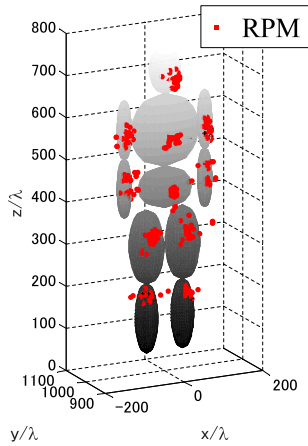


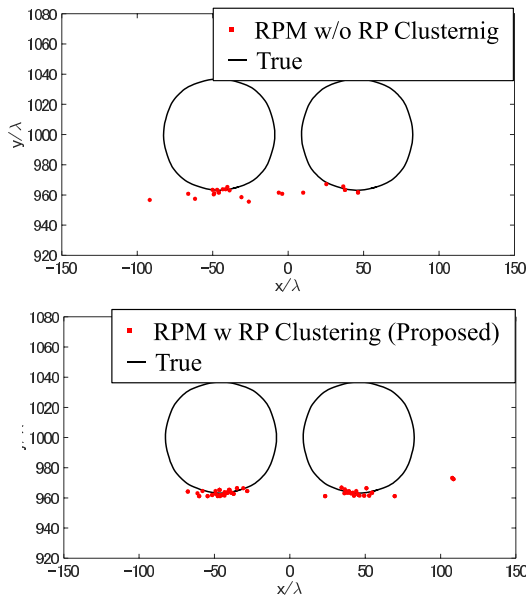
Fig. 7 Target points obtained by the original multi-static RPM method in noiseless case.

image reconstruction in order to obtain the highest accuracy. Furthermore, this figure indicates that there are unnecessary and periodical responses far from the actual target boundaries, which are caused by grating lobes. Moreover, it costs around 300 hours to reconstruct a full 3-D image with Intel Xeon CPU E5-1620 (3.6 GHz) with  $1.0$  voxel spacing for the range  $-150\lambda \leq x \leq 150\lambda$ ,  $900\lambda \leq y \leq 1100\lambda$ ,  $0\lambda \leq z \leq 800\lambda$ . Note that other computationally efficient SAR imaging algorithms, such as  $\omega$ - $k$  migration could not completely solve the problem.

In contrast, Fig. 7 shows the target points obtained by the conventional multistatic RPM method and the proposed RPM method. Figure 8 shows the image obtained by the proposed method, where the RPM was applied three times. Note that, the same post-processing used for eliminating isolated points [13] is applied to both the conventional and proposed cases. These results denote that the proposed



**Fig. 8** Target points obtained by the proposed RPM method in noiseless case.



**Fig. 9** Cross-section images obtained by the original RPM (Upper) and the proposed RPM (Lower).

method offers more accurate 3D imaging by introducing range-points clustering. In terms of computational cost, the conventional method requires 647 s to generate the full 3D image. However, the proposed method requires 450 s even with three times the iterations. Figure 9 show the cross-section images generated by the conventional RPM and the proposed method. This comparison verifies that the proposed method enhances the accuracy without sacrificing the computational cost by applying the range-points clustering scheme. The reason for the improvement in the accuracy is that the SubRPs derived from the different target clusters would degrade the reconstruction accuracy in the RPM process as discussed in Sect. 4.1. For instance, the MainRP designated as target #1 in Fig. 3 should be processed by only the SubRPs associated with target #1. Since the SubRPs associated with different targets (e.g., #2 or #3) have no infor-

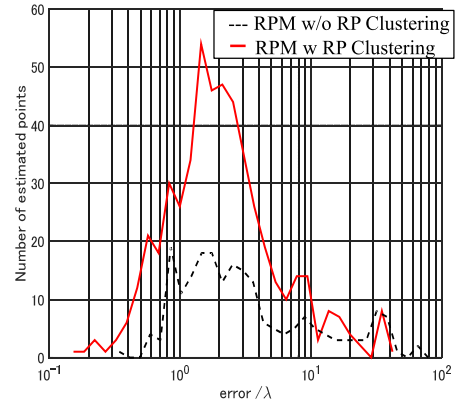


**Fig. 10** Distribution of imaging errors for each method.

mation about target #1, these SubRPs could not contribute to the reconstruction of that target boundary point. Here, the SAR, the original RPM, and the proposed method could reconstruct a small portion of each ellipsoid boundary. This is because, in this case, the aperture angle (determined by the aperture size and the distance to target) is small. This property is a common problem in any imaging algorithm, and it should be resolved by a post-processing scheme. One possible solution is to exploit the motion of the target, if the target motion is given or estimated, the equivalent aperture size can be expanded [14]. This would be similar to the Inverse SAR process. Another possible solution is the model-based extrapolation scheme, which has been used for ellipsoid fitting [15] and exploiting a full polarimetric data analysis [16].

Here, the accuracy in this reconstruction is defined as being the position error of the reconstructed scattering center from the actual boundary. For the quantitative evaluation, the reconstruction error, denoted by  $e(\mathbf{p}_i^{\text{est}})$  is introduced as follows:

$$e(\mathbf{p}_i^{\text{est}}) = \min_{\mathbf{p}^{\text{true}}} \|\mathbf{p}_i^{\text{est}} - \mathbf{p}^{\text{true}}\|_2, \quad (i = 1, 2, \dots, N_T), \quad (8)$$

where  $\mathbf{p}_i^{\text{est}}$  and  $\mathbf{p}^{\text{true}}$  are a location of the  $i$ -th estimated and true target points, respectively.  $N_T$  is the total number of  $\mathbf{p}_i^{\text{est}}$ . Figure 10 shows the histogram of this error value for the two methods, and shows that the number of target points calculated by the conventional method is considerably lower than that of the proposed method. This is because the conventional method generates large erroneous target points, which have been eliminated by post-processing (isolated points elimination) [13]. In contrast, the proposed method retains the number of target points, each of which expresses independent information about the target boundary. Specifically, it shows that the proposed method can increase the accurate target points considerably more than the RPM without range points clustering can. The total number of target points is 211 (55.8%) by the conventional RPM and 370 (90.0%) by the proposed RPM. Figure 11 shows the cumulative distribution of the error value in each method. This result shows that 84% of the target points obtained by RPM satisfies  $e(\mathbf{p}_i^{\text{est}}) < 10\lambda$ . On the contrary, 93% of those ob-

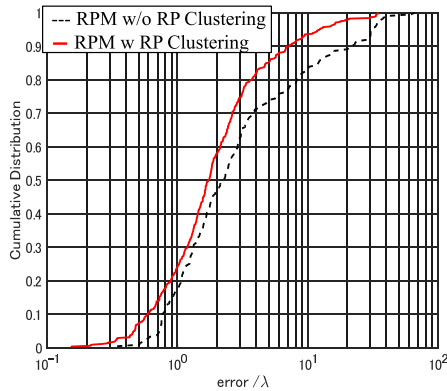


**Fig. 11** Cumulative distribution for imaging errors for each method.

tained by the proposed method satisfies  $e(\mathbf{p}_i^{\text{est}}) < 10\lambda$ . Contrarily, 93% of those obtained by the proposed method satisfies  $e(\mathbf{p}_i^{\text{est}}) < 10\lambda$  (around 20 mm in this model). This evaluation quantitatively verifies the effectiveness of the proposed method in terms of reconstruction accuracy without increasing the computational cost. While a direct and fair comparison between RPM and SAR images is difficult because of the difference in the reconstruction expression, it is obvious that RPM does not generate any false images because of the grating lobe; this is because RPM is not based on a coherent focusing approach. As such, our proposed method has a significant advantage over the conventional DAS-based method.

## 5.2 Noisy Case

Here, we investigate the performance under increased noise. Gaussian white noises are added to the received signals. S/N is defined as the ratio of the peak instantaneous signal power to the average noise power after applying a matched filter, which is a most strict definition considering the locality of the received signal both in time and frequency. Figures 12 and 13 show the image generated by the conventional RPM and the proposed RPM, respectively, at S/N = 30 dB. These figures show that target points become less than those when there is no noise, because the spatially isolated points, namely, large error-estimated points are eliminated during postprocessing. Furthermore, the imaging accuracy is statistically investigated through the Monte Carlo simulation, where 100 different noise patterns are tested. On average, the proposed method recovers the total accurate target points to 67.6% (136 points), compared with those obtained using the original RPM (15.7%; 42 points). In the cumulative distribution of the error value in each method, 49.2% of the target points obtained by RPM satisfies  $e(\mathbf{p}_i^{\text{est}}) < 10\lambda$ . 73.2% of those obtained by the proposed method satisfy  $e(\mathbf{p}_i^{\text{est}}) < 10\lambda$  (approximately 20 mm in this model). In average, the error value of target points obtained by RPM is  $34.82\lambda$ . On the contrary, that of proposed method is  $7.76\lambda$ . This evaluation also verifies the effectiveness of the proposed method in terms of reconstruction accuracy and recovered accuracy.

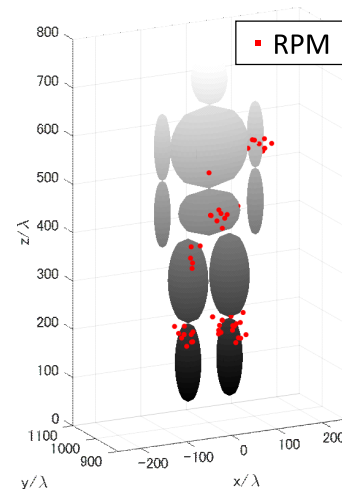


**Fig. 12** Target points obtained by the original multi-static RPM method (noisy case).

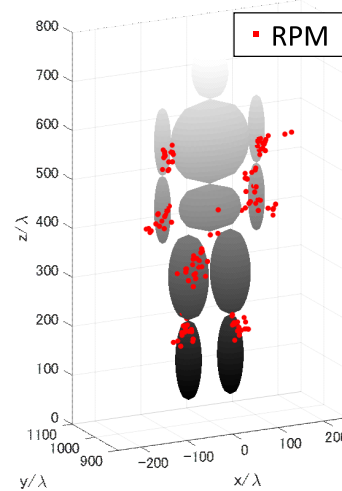


**Fig. 13** Target points obtained by the proposed RPM method (noisy case).

## 6. Conclusion

We propose a high-speed and accurate 3D imaging method for short-range UWB radars, where the range-points clustering process is added to the RPM method to enhance reconstruction accuracy and reduce computation cost. To implement range-points clustering without any prior knowledge of the target shape or location, first, a set of range points is selected (much less than all range points). Then, all the range points are clustered by exploiting the unique feature of the RPM offering one-to-one correspondence between the target and the range points. Furthermore, to enhance accuracy, the RPM and RP clustering processes are iteratively performed, where the clustering information is sequentially updated. The results of numerical simulations with GO approximation, demonstrate that the preclustering significantly reduces computational time and that the itera-

tive approach remarkably enhances the reconstruction accuracy. As the assumed array setting provided an insufficient aperture angle, the reconstructed image could not contain a whole human body. In future, we intend to combine the motion estimation for expanding the aperture size and the extrapolation scheme, as discussed in Sect. 5.1. In this simulation, the received data is generated by a geometrical optics approximation (GO) due to a much higher frequency (140 GHz) radar scenario. Although GO is only applicable in the case where the roughness of the target surface is sufficiently larger than that of the assumed wavelength, each surface of the assumed ellipsoids satisfies this condition; thus, the discussion of an actual scenario is not ideal. However, GO is hardly satisfactory to use in a case where an actual human body is used. To generate more relevant data, a finite-difference time-domain-based simulation should be used; we will look to use this in future investigations. Furthermore, experiments using 140 GHz modules would also be within this scope.

### Acknowledgments

This work is supported by the project “140 GHz band accurate radar system” promoted by Japanese Ministry of Internal Affairs and Communications, Japan.

### References

- [1] A.J. Devaney, “Time reversal imaging of obscured targets from multistatic data,” *IEEE Trans. Antennas Propag.*, vol.53, no.5, pp.1600–1610, May 2005.
- [2] J. Song, Q.H. Liu, P. Torrione, and L. Collins, “Two-dimensional and three dimensional NUFFT migration method for landmine detection using ground-penetrating radar,” *IEEE Trans. Geosci. Remote Sens.*, vol.44, no.6, pp.1462–1469, June 2006.
- [3] T. Sakamoto and T. Sato, “A target shape estimation algorithm for pulse radar systems based on boundary scattering transform,” *IEICE Trans. Commun.*, vol.E87-B, no.5, pp.1357–1365, May 2004.
- [4] K. Saho, T. Sakamoto, T. Sato, K. Inoue, and T. Fukuda, “Accurate and real-time pedestrian classification based on UWB Doppler radar images and their radial velocity features,” *IEICE Trans. Commun.*, vol.E96-B, no.10, pp.2563–2572, Oct. 2013.
- [5] K. Saho, H. Homma, T. Sakamoto, T. Sato, K. Inoue, and T. Fukuda, “Accurate image separation method for two closely spaced pedestrians using UWB Doppler imaging radar and supervised learning,” *IEICE Trans. Commun.*, vol.E97-B, no.6, pp.1223–1233, June 2014.
- [6] S. Kidera, T. Sakamoto, and T. Sato, “Accurate UWB radar 3-D imaging algorithm for complex boundary without wavefront connection,” *IEEE Trans. Geosci. Remote Sens.*, vol.48, no.4, pp.1993–2004, April 2010.
- [7] R. Salman and I. Willms “3D UWB radar super-resolution imaging for complex objects with discontinuous wavefronts,” *IEEE International Conference on Ultra-Wideband (ICUWB) 2011*, pp.346–350, 2011.
- [8] S. Shaghayegh, F. Jian, and Y. Hoi-Shun Lui, “UWB SAR imaging of near-field object for industrial process applications,” *Proc. IEEE, 2013 7th European Conference on Antenna and Propagation (EuCAP)*, 2013.
- [9] H. Taki, S. Tanimura, T. Sakamoto, T. Shiina, and T. Sato, “Accurate ultrasound imaging based on range point migration method for the depiction of fetal surface,” *The Japan Society of Ultrasonics in Medicine 2014*, pp.51–58, Sept. 2014.

- [10] T. Sakamoto, T. Sato, P. Aubry, and A. Yarovoy, “Fast imaging method for security systems using ultrawideband radar,” *IEEE Trans. Aerosp. Electron. Syst.*, vol.52, no.2, pp.658–670, April 2016.
- [11] R. Yamaguchi, S. Kidera, and T. Kirimoto, “Nonparametric UWB radar imaging algorithm for moving target using multi-static RPM approach,” *Asia-Pacific Conference on Synthetic Aperture Radar (APSAR) 2011*, pp.275–278, Seoul, Korea, Sept. 2011.
- [12] D.L. Mensa, G. Heidbreder, and G. Wade, “Aperture synthesis by object rotation in coherent imaging,” *IEEE Trans. Nucl. Sci.*, vol.27, no.2, pp.989–998, April 1980.
- [13] Y. Sasaki, S. Kidera, and T. Kirimoto, “Accurate 3-D imaging method based on range points migration for 140 GHz-band radar,” *IEEE International Conference on Ubiquitous Wireless Broadband (ICUWB) 2015*, Montreal, Canada, Oct. 2015.
- [14] R. Yamaguchi, S. Kidera, and T. Kirimoto, “3-dimensional imaging and motion estimation method of multiple moving targets for multi-static UWB radar using target point and its normal vector,” *IEICE Trans. Commun. E97-B*, no.12, pp.2819–2829, Dec. 2014.
- [15] Y. Abe, S. Kidera, and T. Kirimoto, “Accurate image expansion method using range points based ellipse fitting for UWB imaging radar,” *IEICE Trans. Commun.*, vol.E95-B, no.7, pp.2424–2432, July, 2012.
- [16] A. Yamaryo, S. Kidera, and T. Kirimoto, “3-dimensional image expansion method by incorporating RPM imaging and full polarimetric data for UWB short range radar,” *Proc. 2015 IEEE International Conference on Ubiquitous Wireless Broadband (ICUWB2015)*, Oct. 2015.



**Yuta Sasaki** received the B.E. degree in Mechanical Engineering and Intelligent Systems from The University of Electro Communications in 2014. He is currently studying M.E degree in Mechanical Engineering and Intelligent Systems at the Graduate School of Informatics and Engineering, University of Electro-Communications.



**Fang Shang** received the B.S. and M.S. degree in electrical engineering and automation from Harbin Institute of Technology, China, in 2009 and 2011. She received the Ph.D. degree in electrical engineering and information systems from The University of Tokyo, Japan, in 2014. She is an Assistant Professor in the Graduate School of Informatics and Engineering, University of Electro-Communications, Japan. Her current research interest is in the signal and imaging processing for the polarimetric SAR

and the UWB radar.



**Shouhei Kidera** received his B.E. degree in Electrical and Electronic Engineering from Kyoto University in 2003 and M.I. and Ph.D. degrees in Informatics from Kyoto University in 2005 and 2007, respectively. He is currently an Associate Professor in Graduate School of Informatics and Engineering, the University of Electro-Communications, Japan. His current research interest is in advanced radar signal processing or electromagnetic inverse scattering issue for ultra wideband (UWB) sensor. He was

awarded Ando Incentive Prize for the Study of Electronics in 2012, Young Scientists Prize in 2013 by the Japanese Minister of Education, Culture, Sports, Science and Technology (MEXT), and Funai Achievement Award in 2014. He is a member of the Institute of Electrical and Electronics Engineering (IEEE) and the Institute of Electrical Engineering of Japan (IEEJ).



**Tetsuo Kirimoto** received the B.S. and M.S. and Ph.D. degrees in Communication Engineering from Osaka University in 1976, 1978 and 1995, respectively. During 1978–2003 he stayed in Mitsubishi Electric Corp. to study radar signal processing. From 1982 to 1983, he stayed as a visiting scientist at the Remote Sensing Laboratory of the University of Kansas. From 2003 to 2007, he joined the University of Kitakyushu as a Professor. Since 2007, he has been with the University of Electro-Communications, where

he is a Professor at the Graduate School of Informatics and Engineering. His current study interests include digital signal processing and its application to various sensor systems. Prof. Kirimoto is a senior member of IEEE and a member of SICE (The Society of Instrument and Control Engineers) of Japan.